SUPPLEMENTARY INFORMATION
DOI: 10.1038/NNANO.2016.85

Coherent commensurate electronic states at the interface between misoriented graphene layers

Elad Koren*, Itai Leven, Emanuel Lörtscher, Armin Knoll, Oded Hod and Urs Duerig*

*Email: elk@zurich.ibm.com, drg@zurich.ibm.com

Content:

1. Rotation actuation.

2. Selection of pillar dimensions.

3. Interface conductivity measurement.

4. Bias dependence of the interface conductivity.

5. Double peak structures for SE-even interface stacking.

6. Phonon mediated transport calculations.

7. Electronic transport calculations.

8. Registry index calculations.

9. References.

© 2016 Macmillan Publishers Limited. All rights reserved.

DOI: 10.1038/NNANO.2016.85

1. Rotation actuation

A force F_{tip} is applied to the lever arm section at an off-center position, $r_{tip,}$, by slowly moving the tip on a circular track around the center position of the circular mesa section. The force gives rise to a torque $M = F_{tip}$ x r_{tip} and a lateral shear force F_{tip} acting at a center position. As shown in Ref. (*1*) a glide plane defect is spontaneously created within the mesa if the shear force exceeds a threshold of $F_{tip} > 2\sigma r \approx 150$ nN where $\sigma = 0.227$ Nm^{-1} is the interface tension between two graphene sheets and r = 330 nm is the radius of the cylindrical mesa section. The top mesa section is essentially free to rotate around the center axis and to glide along the direction of the applied force as soon as the glide plane defect has been created. The translational glide motion is, however, inhibited by counterbalancing adhesive line tension forces (*1*) which stabilize the rotation axis at a center position (Fig. S1).

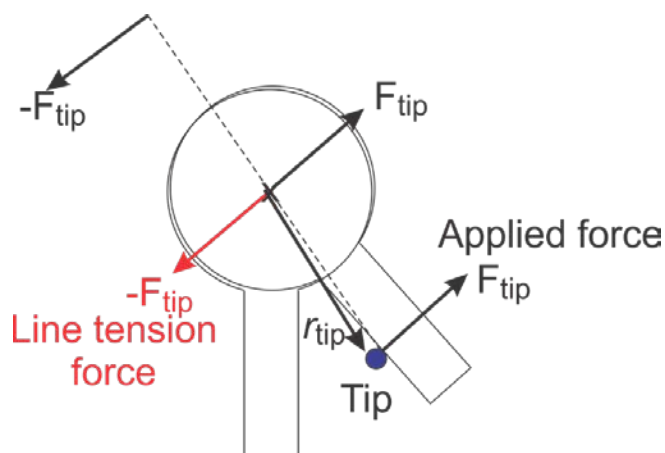

Supplementary Figure 1 | Schematic of the rotation actuation and axis stabilization at a center position of the cylindrical mesa section.

The rotation can be performed with virtually zero applied force except for the high symmetry points at multiple integers of 60º where a locking force on the order 1 µN has been observed. Unfortunately, we can only qualitatively assess the lateral tip force during the experiment because the lateral cantilever deflection axis is in general not orthogonal to the circular tip trajectory. The tip rotation can be stopped at will and the

© 2016 Macmillan Publishers Limited. All rights reserved.

structure can be imaged in the tapping mode after retraction of the tip as shown in Fig. 1c for the high symmetry rotation angles and for the commensurate angles of 21.8º and 38.2º. Note that in all cases the circular mesa sections of the rotated and the fixed structure overlap after performing the rotation manipulation.

In practice, we record the time trace of the current during the rotation using a digital oscilloscope. Hence, it is required to convert the current trace from temporal to angular units. During the rotation the cantilever moves with a constant angular velocity, determined by the user. The precise angular velocity is determined by considering the ratio between the angular displacement $\Delta\theta$ and the duration Δt which it takes to complete the circular motion. The following equation is used for the unit conversion:

$$\theta = t \times \frac{\Delta\theta}{\Delta t} \qquad (S1)$$

Δt is extracted from the time trace signal of the x-y piezo sensors (Fig. S2). $\Delta\theta$ is entered as an input to the control software and the rotation is executed from a tip starting (x1,y1) position and ending at (x2,y2) on a circular path with radius r_{scan} (inset in Fig. S2).

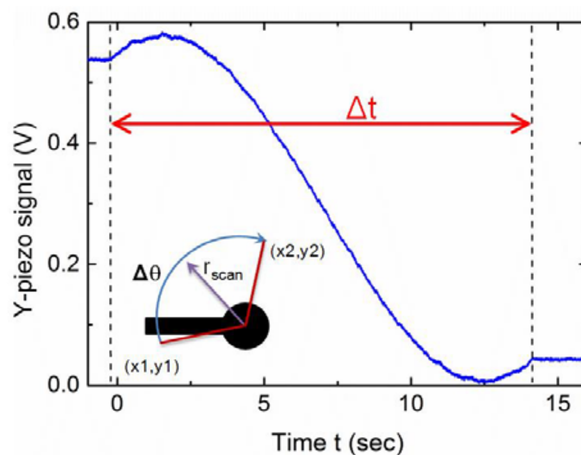

Supplementary Figure 2 | Measured time trace of the y-piezo signal, taken from the oscilloscope during a 180°rotation. The red arrow marks the time interval Δt which it takes to complete the full rotation.

© 2016 Macmillan Publishers Limited. All rights reserved.

DOI: 10.1038/NNANO.2016.85

2. Selection of pillar dimensions

When selecting the optimal pillar radius one should balance between the ability to form the glide plane defect and the need to stabilize the rotation axis. On one hand, we have previously shown (Ref. 1) that at pillar radii exceeding 400 nm it becomes impractical to induce the glide plane defect via external manipulations. This sets an upper limit on the relevant pillar radii. On the other hand, large pillar radii are favorable as their enhanced interplanar adhesion stabilizes the rotation axis at the center of the pillar. Such stabilization is crucial as the actuation force is applied asymmetrically at an off-center position (see Fig. S1) in order to form the initial glide plane and to induce the rotational motion This in turn gives rise to a lateral force of equal magnitude acting at the center of the pillar structure that must be counterbalanced by the interfacial line tension forces in order to prevent the mobile upper pillar section from being pushed off the fixed bottom part. Here, it was found that pillars with radii below 200 nm do not provide sufficient stabilization of the rotation axis thus providing a lower bound on the relevant pillar radii. Based on these findings, we chose a pillar radius of 330 nm that allows for the formation of the glide plane defect and provides sufficient stabilization of the rotation axis. The pillar height of 50 nm is chosen since it provides a sufficiently low and adequately defined pillar resistance of ~600 Ω (see Ref. 2) that is also much larger than the spreading resistance of ~ 30 Ω (see Ref. 3).

The length of the lever arm was chosen to be 1 μm as a compromise between the need to minimize the actuation force by extending the lever arm and structural stability provided by shorter arms. In this respect, it is critical that the lever arm does not touch the graphite substrate during rotation. This is readily achieved with the chosen structure for rotation angles covering a full 60º range but it is much more challenging for rotation angles exceeding 120º. We note however that the measured profiles exhibit a six fold rotational symmetry (see Fig. S3), as expected from the underlying hexagonal lattices, hence a 60º rotational angle range provides all the required information.

© 2016 Macmillan Publishers Limited. All rights reserved.

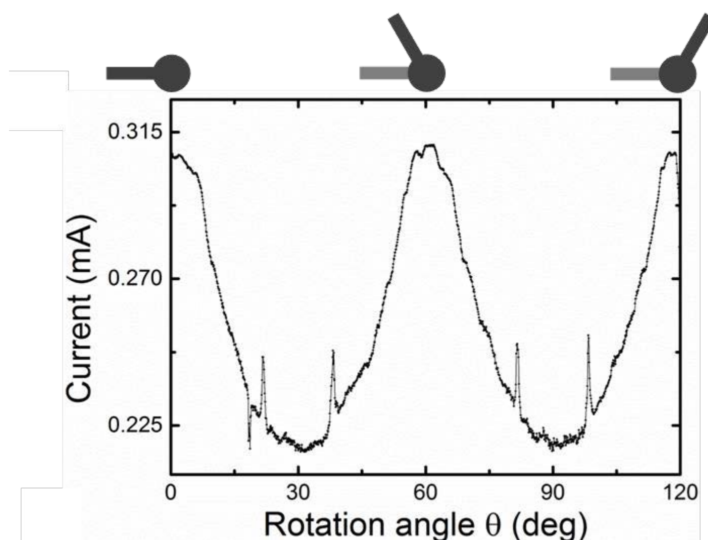

Supplementary Figure 3| Current measured at a bias potential of 0.5 V and over a 120º angular range.

3. Interface conductivity measurement

The current flowing through the pillar is measured by means of a virtual ground type current-to-voltage converter connected to the HOPG substrate while applying a bias potential V to the cantilever (Fig. S4a).

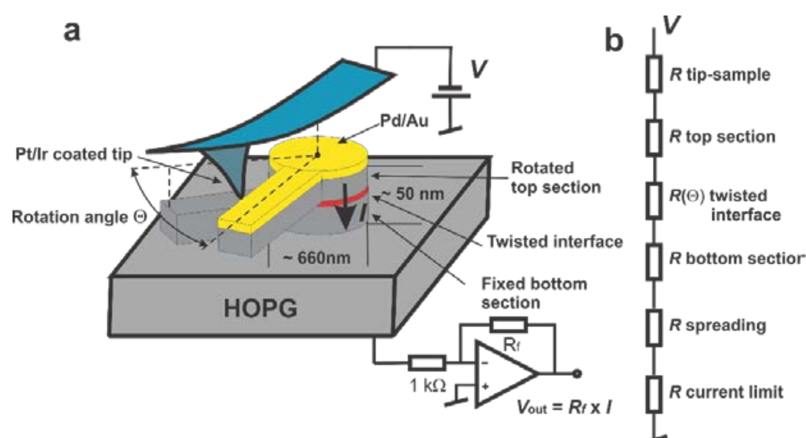

Supplementary Figure 4| **(a)** Schematic of the electrical transport measurement setup. **(b)** Equivalent electrical circuit comprising constant resistance elements representing the tip-sample contact resistance, the resistance of the HOPG top section of the mesa, the resistance

© 2016 Macmillan Publishers Limited. All rights reserved.

DOI: 10.1038/NNANO.2016.85

of the HOPG bottom section of the mesa, and spreading resistance to the HOPG substrate, and the angular dependent resistance element $R(\theta)$ of the twisted interface.

As mentioned in the main text, the overall measured electrical resistance $R_T(\theta) = R_{CL} + R_P + R_{t-s} + R_{int}(\theta)$ for a given angular configuration θ is composed of the current limiting resistor $R_{CL} = 1\ k\Omega$ and the serial elements R_P, R_{t-s}, and $R_{int}(\theta)$ (Fig. S4b). $R_P \approx 450\Omega$ denotes the c-axis resistance of the graphite pillar which is composed of the rotated top and fixed bottom section including the spreading resistance, $R_S \approx 30\Omega$ *(3)*, into the HOPG substrate at the bottom of the pillar, $R_{t-s} \approx 270\Omega$ denotes the tip-sample contact resistance which is dominated by the electrical resistance of the cantilever probe *(2)*, and $R_{int}(\theta)$ denotes the resistance of the twisted interface. We consider R_P and R_{t-s} to be constant throughout the rotation. Therefore, the twisted interface resistance can be evaluated by subtracting the constant resistance $R_C = R_{CL} + R_P + R_{t-s}$ from the total resistance i.e. $R_T(\theta) - R_C = R_{int}(\theta)$. However, the large scatter of measured c-axis resistance values in meso-scale graphite samples (*2*,*3*) relative to the low resistance of $R_{int}(\theta = 0)$ yields considerable unknown systematic errors for $R_{int}(\theta)$. Therefore we fix the interface resistance at θ = 0º to the value of the resistance corresponding to a stacking fault defect $R_{sf} = R_{int}(\theta = 0) = \rho_{sf}/\pi r^2 \cong 50\ \Omega$ where $\rho_{sf} \cong 1.5 \times 10^7\ \Omega\ \text{nm}^2$ is the specific stacking fault resistivity (*2*), and r = 330 nm is the radius of the circular pillar. This allows us to extract the twisted interface resistance $R_{int}(\theta) = R_T(\theta) - R_C$ and the interface conductivity $\sigma_{int}(\theta) = (R_{int}(\theta) \times \pi r^2)^{-1}$ for the entire angular range using $R_C \cong R_T(\theta = 0) - 50\ \Omega$. The approach is motivated by the fact that the creation of a glide plane defect always involves a minor translational motion on the order of nanometers.

We note that our analysis method cannot account accurately for the absolute interface resistance for 0°, but it rather represents an upper limiting value. If we were to estimate the interface resistance from the c-axis resistivity $\rho_c \approx 4 \times 10^{-3}\Omega\text{m}$ we would obtain $R_{int}(\theta = 0) = \rho_c\ d/\pi r^2 \approx 4\ \Omega$ where d = 0.34 nm is the distance between graphite layers. The choice of the value of the interface resistance at $\theta = 0$ has only a minor effect on the conductivity profile for angular configurations > 5°, however (Fig. S5).

© 2016 Macmillan Publishers Limited. All rights reserved.

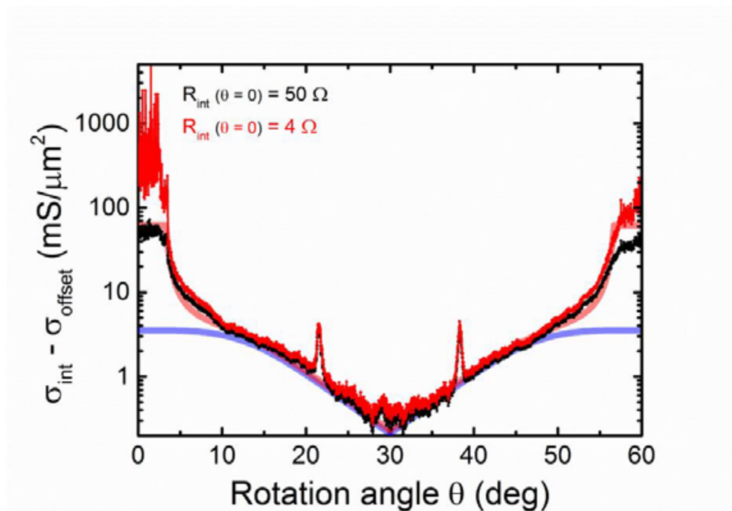

Supplementary Figure 5 | A comparison between $R_{int}(\theta)$ when considering two different values for $R_{int}(\theta = 0)$. The main deviation between the black ($R_{int}(\theta = 0) = 50\ \Omega$) and red ($R_{int}(\theta = 0) = 4\ \Omega$) profiles appears at angles < 3° i.e. in the plateau regime.

4. Bias dependence of the interface conductivity

We apply a fixed external bias potential, V, in our twist experiments. However, the actual interface potential, V_{int}, depends on the rotation angle due to the angular dependence of the interface resistance, R_{int}, which is part of a voltage divider network formed by the various series resistance elements as discussed in section 3. The voltage drop at the interface is given by

$$V_{int}(\theta) = V \frac{R_{int}(\theta)}{R_0 + R_{int}(\theta)} \qquad (S2)$$

with

$$R_0 = \frac{V}{I_0} - R_{sf} \qquad (S3)$$

where I_0 is the current measured at zero degree rotation and the interface resistance at zero degree rotation is normalized to the stacking fault resistance $R_{sf} \approx 50\ \Omega$ (see section 3). Eqn (S2) can be rewritten in terms of interface conductivity, σ_{int},

$$V_{int} = V \frac{1}{1 + R_0 A \sigma_{int}(\theta)} \qquad (S4)$$

where $A = \pi r^2 \approx 0.34\ \mu m^2$ is the pillar cross section.

The resistance of the HOPG pillar is given by $R_P = R_0 - 1.27\ k\Omega$ (see section 2). With $R_P \approx 456\pm28\ \Omega$, see Table 1, which is within the tolerance expected from the pillar

© 2016 Macmillan Publishers Limited. All rights reserved.

 DOI: 10.1038/NNANO.2016.85

height and radius uncertainties and the fundamental variance of the resistivity in these structures (2), one finds a typical value of $R_0 \approx 1.72 \pm 0.03$ kΩ, see Table S1. Accordingly the interface potential can be approximately written in the form

$$V_{int} \approx V \frac{1}{1 + 0.58mS^{-1}\mu m^2 \sigma_{int}(\theta)} \quad . \qquad (S5)$$

Referring to the data shown in Fig. 2 a) and b) in the main text corresponding to V = 50 mV one finds that the interface potential is on the order of 24 mV at the conductivity minimum at 30º and 12 mV at the commensurate peaks with σ_{peak} = 3.55±0.3 mSμm^{-2}.

The phonon fit parameters and the commensurate peaks are perfectly reproducible among the different samples as shown in Fig. S6 measured at a bias of 50 mV. Furthermore, these parameters do not depend on the applied bias as shown in Tables S1 and S2. However, the offset conductivity is clearly bias dependent. Fig. S7 shows current and conductivity data pertaining to Figs 2 c) and d) in the main text measured at V = 0.25 V. The offset conductivity σ_{offset} = 2.65±0.1 mSμm^{-2} has increased by 0.95 mS with respect to the value σ_{offset} = 1.7±0.15 mSμm^{-2} obtained at V = 50 mV. However, the angle dependent part of the conductivity is reproduced with excellent fidelity by the phonon transport model with virtually identical parameters, see Table S1. Likewise, we obtain the same values within statistical uncertainty for the conductivity at the commensurate peaks, σ_{peak} = 3.9±0.6 mSμm^{-2}, as in the low bias experiments, σ_{peak} = 3.55±0.3 mSμm^{-2}, see Table S2. This further underlines the robustness of the reported results in view of the fact that the interface potential differs by approximately a factor of 4 between the data sets obtained at 50 mV and 0.25 V.

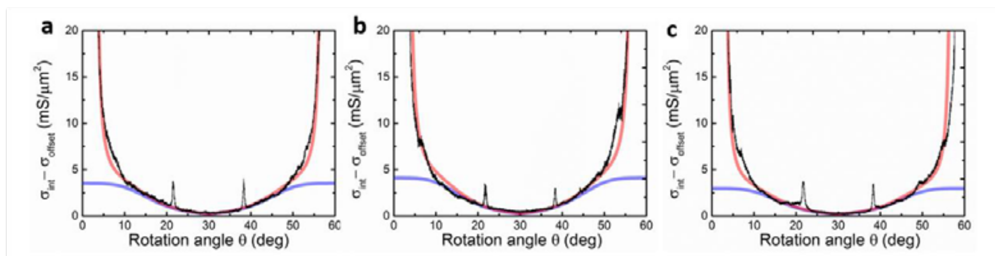

Supplementary Figure 6 | Interface conductivity determined from current measurements at a bias of 50 mV for three different pillar samples shown in Fig 2 a) in the main text: **a**, **b**, and **c**

© 2016 Macmillan Publishers Limited. All rights reserved.

correspond to the data shown in black, blue and red in Fig. 2 a). Fits of to the phonon mediated transport model without and including Fermi velocity renormalization are shown as blue and red lines, respectively. The corresponding fit parameters and offset conductivities are listed in Table S1.

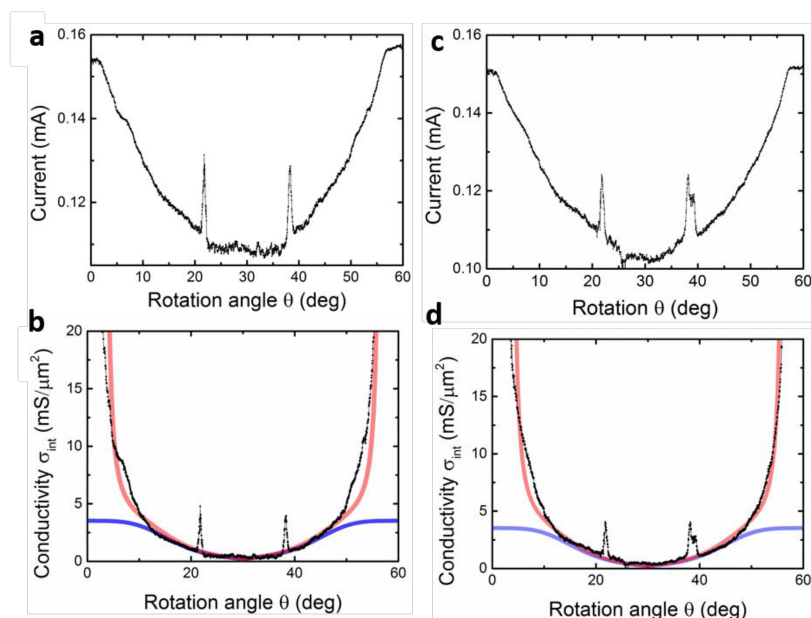

Supplementary Figure 7 | Measured current at a bias of 250 mV and corresponding interface conductivity for the data shown in Fig. 2 c), panels **a** and **b**, and Fig. 2 d), panels **c** and **d**, in the main text. The data has been obtained from two different pillar samples. Fits of to the phonon mediated transport model without and including Fermi velocity renormalization are shown as blue and red lines, respectively. The corresponding fit parameters are listed in Table S1.

	Bias voltage V (V)	Interface bias at θ=30° (mV)	Total resistance V/I(0°) and R_0 (Ohm)	Pillar resistance R_P (Ohm)	Offset conductivity σ_{offset} (mSμm^{-2})	Fermi energy E_F (eV)	Transverse hopping integral $t_\perp$ (eV)	Phonon conductivity at 30° σ_{ph} (mSμm^{-2})
Sample 1, Fig. S6 a Fig. 2a (red)	0.05	24	1833 1783	513	1.55	0.12±0.02	0.18±0.05	0.20
Sample 2, Fig. S6 b Fig. 2a (blue)	0.05	24	1753 1703	433	1.65	0.13±0.02	0.20±0.05	0.27
Sample 3, Fig. S6 c Fig. 2a (black), b	0.05	22	1763 1713	443	1.9	0.12±0.02	0.18±0.05	0.23
Sample 4, Fig. S7 b	0.25	91	1755 1705	435	2.75	0.13±0.02	0.20±0.05	0.25

© 2016 Macmillan Publishers Limited. All rights reserved.

 DOI: 10.1038/NNANO.2016.85

Fig. 2c								
Sample 5, Fig. S7 d Fig. 2d	0.25	96	1780 1730	460	2.55	0.11±0.02	0.22±0.05	0.18
Mean value		23±0.1 93.5±0.25	R_0=1720±30	456±28	1.7±0.15 2.65±0.1	0.122±0.008	0.196±0.01	0.226±0.03

Supplementary Table 1 | Electrical and fit parameters referring to the samples indicated in the table. The variances quoted for the Fermi energy and the transverse hopping integral refer to the fit uncertainties. The mean values of the parameters are shown in the row labelled "Mean". The uncertainties correspond to the standard deviation observed in different samples. The phonon conductivity at θ=30º is calculated using the fit eqn(S6). The interface potential is calculated by means of eqn (S4) with $\sigma_{int} = \sigma_{offset} + \sigma_{ph}(30º)$.

	Sample 1, Fig. S6 a Fig. 2a (red)	**Sample 2, Fig. S6 b Fig. 2a (blue)**	**Sample 3, Fig. S6 c Fig. 2a (black), b**	**Sample 4, Fig. S7 b Fig. 2c**	**Sample 5, Fig. S7 d Fig. 2d**
Bias voltage V (V)	0.05	0.05	0.05	0.25	0.25
peak conductivity σ_{peak} (mSμm^{-2}) (mSμm^{-2}) θ = 21.8º	3.7	3.5	3.7	5.0	3.3
Interface potential at peak (mV) θ = 21.8º	12	12.5	15	45.5	56
peak conductivity σ_{peak} (mSμm^{-2}) θ = 38.2º	4.0	3.0	3.4	3.9	3.5
Interface potential at peak (mV) θ = 38.2º	11	13.5	12	51.5	55
mean value of peak conductivity σ_{peak} (mSμm^{-2})	3.55±0.3			3.9±0.6	
mean value of peak conductivity $V \leq 0.25$ V σ_{peak} (mSμm^{-2})	3.7 ±0.5				

Supplementary Table 2 | Peak conductivity and interface potential calculated by means of eqn (S4) with $\sigma_{int} = \sigma_{offset} + \sigma_p$ referring to the samples indicated in the table. The uncertainties correspond to the standard deviation observed in different samples. Note that the peak conductivity does not depend on the sample bias within the statistical errors.

© 2016 Macmillan Publishers Limited. All rights reserved.

One may wonder about the justification of a constant offset subtraction in the data analysis given the apparent bias dependence. We find, however, that for any practical purpose the influence of this procedure on the fit results is marginal. Taking the 0.25 V data as reference, we note that one obtains an offset conductivity of 2.65 mSμm^{-2} at an interface potential of 93.5 mV (see Table S1). To reduce the offset conductivity by 1 mSμm^{-2} the interface potential would have to be ~ 23 mV (see Table S1). For a bias of 0.25 V this low value of the interface potential is obtained at an interface conductivity of σ_{int} = 17 mSμm^{-2} (see eqn (S5)) which is much larger than the potential error made by neglecting the bias dependence of the offset and the effect would only be noticeable at small twist angles θ < 5º.

The results of a systematic study of the bias dependence up to 3 V are summarized in Fig. S8 and Table S3. Each data set has been obtained on a different pillar structure. The results first demonstrate that the angle dependent part of the interface conductivity is reproduced by the phonon conduction model up to an interface potential of 0.4 V. Second, the bias dependence of the offset conductivity increases with interface potential, in particular for V_{int} > 0.25 V, which is typical for a tunneling process. Third, the commensurate peak structure becomes invisible as soon as the offset conductivity exceeds ~ 7 mSμm^{-2}.

	Bias voltage V **(V)**	**Interface bias at θ=30º (V)**	**Total resistance** V/I**(0º) and** R_0 **(Ohm)**	**Pillar resistance** R_P **(Ohm)**	**Offset conductivity** σ_{offset} **(mSμm^{-2})**	**Fermi energy** E_F **(eV)**	**Transverse hopping integral** $t_\perp$ **(eV)**	**Phonon conductivity at 30º** σ_{ph} **(mSμm^{-2})**
Sample 6	0.05	0.022	1763 1713	443	1.9	0.12	0.18	0.23
Sample 7	0.25	0.093	1801 1751	481	2.6	0.12	0.18	0.23
Sample 8	0.5	0.16	1720 1670	400	3.5	0.12	0.18	0.23
Sample 9	1.0	0.27	1660 1610	340	4.5	0.12	0.18	0.23
Sample 10	1.5	0.38	1650 1600	330	5.1	0.12	0.18	0.23
Sample 11	2.0	0.43	1645 1595	325	6.5	0.12	0.18	0.23
Sample 12	2.5	0.45	1660 1610	340	8.2	0.12	0.18	0.23
Sample 13	3.0	0.48	1630 1580	310	9.6	0.12	0.18	0.23

© 2016 Macmillan Publishers Limited. All rights reserved.

 DOI: 10.1038/NNANO.2016.85

Supplementary Table 3 | Electrical and fit parameters (fixed to the values indicated in the table) for the samples in Figure S8. The interface potential is calculated by means of eqn (S4) with $\sigma_{int} = \sigma_{offset} + \sigma_{ph}(30^o)$ where the phonon conductivity is calculated using the fit eqn(S6).

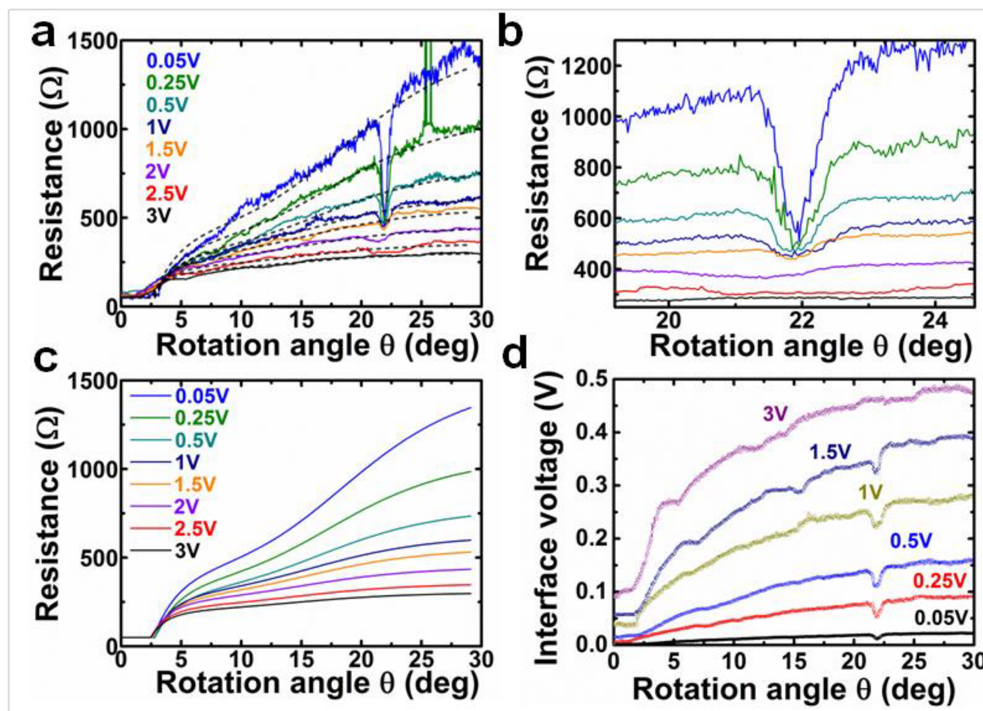

Supplementary Figure 8 | (a) Interface resistance versus rotation angle for 8 different samples measured at different applied potentials ranging from 50 mV to 3 V. Dashed lines correspond to the predicted interface resistance based on an angle dependent phonon contribution and a bias dependent offset conduction (see also panel **c**). The model parameters are given in Table S3. **(b)** Close up view of the same data as in **(a)** in the vicinity of the commensurate angle of 21.8º. The interface resistance at θ = 21.8º does not depend on the bias voltage which gives a strong indication for metallic charge transport mechanism via the commensurate interface state. In contrast, we observe a substantial increase of the offset conductivity with increasing bias potential resulting in a corresponding decrease of the interface resistance at 30º, see Table S3. **(c)** Predicted interface resistance for the different bias potentials assuming an angle dependent but bias independent phonon conduction path and a solely bias dependent parallel conduction path (parameters are quoted in Table S3). **(d)**. Interface bias versus rotation angle calculated by means of eqn (S2).

© 2016 Macmillan Publishers Limited. All rights reserved.

5. Double peak structures for SE-even interface stacking

Double peak structures signaling an SE-even configuration are observed either at 21.8º or at 38.2º in a single rotation experiment, see Fig. S9. There are four fundamental ways to create a commensurate superstructure, (i) an A atom of the substrate overlaps with a B' atom of the rotated structure, (ii) an A atom overlaps with an A' atom, (iii) a B atom overlaps with an A' atom, and (iv) a B atom overlaps with a B' atom. For a rotation angle of 21.8º (i) also implies (iii) leading to a six-fold symmetric SE-even structure whereas for a rotation angle of 38.2º an SE-even structure is obtained for (ii) which also implies (iv). In all other cases the structure will be SE-odd with three fold symmetry. Which of the configurations (i-iv) are realized depends on the position of the rotation axis. Based on the above symmetry property one would expect to find double peaks with ~ 30% probability. However, in reality we observe this structure with a probability of roughly 5% - 10 % (in two cases out of 25 rotation experiments). We think that the strong suppression of SE-even configurations is related to energy barriers emerging at the interface during rotation which lead to slight shifts of the rotation axis which we cannot control.

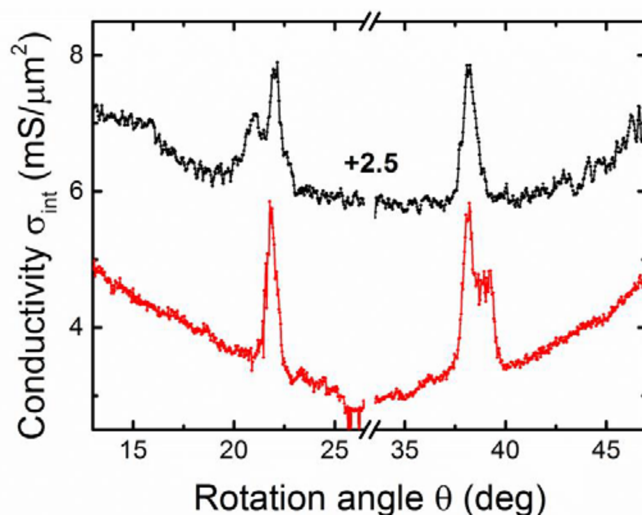

Supplementary Figure 9 | Interface conductivity curves showing double peak structures at 21.8º (black curve, measured at a bias of 25 mV) and at 38.2º (red curve corresponding to the data shown in Fig. 2 d) of the Main text measured at a bias potential of 250 mV). The black curve is offset by 2.5 mSµm^{-2} as indicated in the figure.

© 2016 Macmillan Publishers Limited. All rights reserved.

DOI: 10.1038/NNANO.2016.85

6. Phonon mediated transport calculations

We use the analytical model developed by Perebeinos et al. (*4*) for the phonon mediated interlayer conductivity which is given by

$$\sigma_{ph}(\theta) = 2\pi e^2 g^2 n_\theta E_F^2 A_0/(M_C \omega_\theta \pi^2 \hbar^4 v_F^4) \qquad (S6)$$

where, M_C is the carbon mass, $A_0 = a^2\sqrt{3}/2$ (a being the graphene lattice parameter) is the area of the two-atom cell, $v_F = 10^8\ cm/s$ is the single layer graphene Fermi velocity, n_θ is the thermal population of ω_θ phonons, $g = 0.34\ eV/Å$ is the effective electron-phonon coupling constant. $E_F = \hbar v_F\sqrt{\pi n_s}$ is the Fermi energy for a given electron density n_s. Electrons are predominantly scattered by phonons from the beating mode branch (ZO') of bilayer graphene. The frequency ω_θ of ZO' phonons with momentum $q(\theta) = 2\, q_K \sin\theta/2$ connecting the Fermi circles in the twisted bilayer is given by

$$\omega(\theta) = [\omega_\Gamma^2 + q^4\kappa/\rho]^{1/2} \qquad (S7)$$

where $q_K = 4\pi/3a \cong 17\ nm^{-1}$ is the K point momentum of single graphene layer, $\hbar\omega_\Gamma = 80\ cm^{-1}$ is the zone center beating phonon frequency, $\rho = 7.66 \times 10^{-11}\ Kgcm^{-2}$ is the graphene mass density and $\kappa = 1.66\ eV$ is the effective bending stiffness.

For large twist angles with respect to the high symmetry points at multiples of 60º, i.e. for $10° < \theta < 50°$, an excellent fit of this model to the measured angular dependence of the conductivity is obtained using a constant value of the Fermi velocity $v_F = 10^8\ cm/s$ and $E_F \sim 0.12 \pm 0.01$ eV (for details see section 4). The rapid increase of the interlayer conductivity at low rotation angles is reproduced by considering the renormalized Fermi velocity $\tilde{v}_F$ given by *(5)*

$$\tilde{v}_F/v_F = 1 - 9[\tilde{t}_\perp/(\hbar\, v_F q_K)]^2 \qquad (S8)$$

and using a fixed electron density given by $n_s = (E_F\ /\ \hbar v_F)^2/\pi$. Fits to the data yield a mean value 0.2±0.01 eV for the transverse hopping integral $t_\perp$.

© 2016 Macmillan Publishers Limited. All rights reserved.

7. Electronic transport calculations

For the transport calculations we utilize the Landauer formalism (6) that relates the current and conductance to the transmittance probability, $T(E)$, through the system:

$$I = \frac{2e}{h}\int [f_T(E,\mu_T) - f_B(E,\mu_B)]T(E)dE,$$

$$G = \frac{2e}{h}\int \frac{\partial[f_T(E,\mu_T) - f_B(E,\mu_B)]}{\partial V_b} T(E)\, dE.$$

Here, e is the electron charge, h - Plank's constant, $f_{T/B}(E,\mu_{T/B}) = \left[1 + e^{\beta(E-\mu_{T/B})}\right]^{-1}$ is the equilibrium Fermi-Dirac electronic distribution of the top/bottom lead, $\mu_{T/B} = E_F \pm 0.5V_b$ is the chemical potentials of the top/bottom lead assuming that the bias voltage (V_b) evenly splits between the two leads around the Fermi energy (E_F), and $\beta = (k_B T)^{-1}$ with T being the electronic temperature and k_B Boltzmann's constant. In the conductance equation above, we have neglected the effect of the bias voltage on the electronic structure of the device. In the present case this assumption is reasonable as most of the bias voltage drops across the many stack layers above and below the twisted junction. Furthermore, the metallic nature of the graphene flakes is expected to effectively screen the electric field across the junction before reaching the twisted bilayer region.

The transmittance probability is calculated using the following trace formula of non-equilibrium Green's function formalism:

$$T(E) = Tr\left[\hat{G}_d^R(E)\hat{\Gamma}_B(E)\hat{G}_d^A(E)\hat{\Gamma}_T(E)\right].$$

Here, the top and bottom broadening matrices are given by $\hat{\Gamma}_{T/B} = i\left[\hat{\Sigma}_{T/B}^R - \hat{\Sigma}_{T/B}^A\right]$ and $\hat{\Sigma}_{B/T}^{R/A}$ are the retarded (R) and advanced (A) self-energy terms of the bottom (B) and top (T) leads. Given $\hat{h}_d$ - the Hamiltonian matrix representation of the device, $\hat{G}_d^R(E) = \left[E\hat{I} - \hat{h}_d - \hat{\Sigma}_B^R - \hat{\Sigma}_T^R\right]^{-1}$ represents the retarded Green's function of the device and the advanced counterpart follows the relation $\hat{G}_d^A = \left(\hat{G}_d^R\right)^{\dagger}$.

For the purpose of the present derivation we formally divide the matrix representation of the device's Hamiltonian operator into three blocks in the following manner:

$$\hat{h}_d = \begin{pmatrix} \hat{h}_T^d & \hat{v}_{TC}^d & \hat{v}_{TB}^d \\ \hat{v}_{CT}^d & \hat{h}_C^d & \hat{v}_{CB}^d \\ \hat{v}_{BT}^d & \hat{v}_{BC}^d & \hat{h}_B^d \end{pmatrix},$$

© 2016 Macmillan Publishers Limited. All rights reserved.

DOI: 10.1038/NNANO.2016.85

where $\hat{h}_T^d$ and $\hat{h}_B^d$ are the Hamiltonian matrix blocks of the device's sections that directly couple to the top and bottom leads, respectively, and $\hat{h}_C^d$ is the Hamiltonian block of the central part of the device that is not directly influenced by the leads.

In what follows, we shall replace the leads' self-energies by constant imaginary absorbing potentials acting on $\hat{h}_T^d$ and $\hat{h}_B^d$. (*7,8*) With this we neglect the real part of the self-energies that serves to shift the poles of $\widehat{G}_d^R(E)$ and we assume the wide band approximation such that the imaginary part of the self-energies is replaced by a constant energy independent factor. Furthermore, we assume that the self-energy matrix is diagonal and that all the sites in $\hat{h}_T^d$ or in $\hat{h}_B^d$ experience the same constant broadening as follows:

$$\hat{\Sigma}_T^R = i\gamma_T \begin{pmatrix} \hat{I}_T & \hat{0} & \hat{0} \\ \hat{0} & \hat{0} & \hat{0} \\ \hat{0} & \hat{0} & \hat{0} \end{pmatrix}; \ \hat{\Sigma}_T^A = \left(\hat{\Sigma}_T^R\right)^\dagger = -i\gamma_T \begin{pmatrix} \hat{I}_T & \hat{0} & \hat{0} \\ \hat{0} & \hat{0} & \hat{0} \\ \hat{0} & \hat{0} & \hat{0} \end{pmatrix} = \left(\hat{\Sigma}_T^R\right)^* = -\hat{\Sigma}_T^R,$$

and

$$\hat{\Sigma}_B^R = i\gamma_B \begin{pmatrix} \hat{0} & \hat{0} & \hat{0} \\ \hat{0} & \hat{0} & \hat{0} \\ \hat{0} & \hat{0} & \hat{I}_B \end{pmatrix}; \ \hat{\Sigma}_B^A = \left(\hat{\Sigma}_B^R\right)^\dagger = -i\gamma_B \begin{pmatrix} \hat{0} & \hat{0} & \hat{0} \\ \hat{0} & \hat{0} & \hat{0} \\ \hat{0} & \hat{0} & \hat{I}_B \end{pmatrix} = \left(\hat{\Sigma}_B^R\right)^* = -\hat{\Sigma}_B^R,$$

where γ_T and γ_B are the values of the constant imaginary potentials acting on the top and bottom device sections, respectively, and $\hat{I}_{T/B}$ is a unit matrix of dimensions of the top/bottom lead. The top and bottom broadening matrices can now be calculated as follows:

$$\hat{\Gamma}_T = i\left[\hat{\Sigma}_T^R - \hat{\Sigma}_T^A\right] = i\left[i\gamma_T \begin{pmatrix} \hat{I}_T & \hat{0} & \hat{0} \\ \hat{0} & \hat{0} & \hat{0} \\ \hat{0} & \hat{0} & \hat{0} \end{pmatrix} - (-i\gamma_T) \begin{pmatrix} \hat{I}_T & \hat{0} & \hat{0} \\ \hat{0} & \hat{0} & \hat{0} \\ \hat{0} & \hat{0} & \hat{0} \end{pmatrix}\right] = -2\gamma_T \begin{pmatrix} \hat{I}_T & \hat{0} & \hat{0} \\ \hat{0} & \hat{0} & \hat{0} \\ \hat{0} & \hat{0} & \hat{0} \end{pmatrix}$$

$$\hat{\Gamma}_B = i\left[\hat{\Sigma}_B^R - \hat{\Sigma}_B^A\right] = i\left[i\gamma_B \begin{pmatrix} \hat{0} & \hat{0} & \hat{0} \\ \hat{0} & \hat{0} & \hat{0} \\ \hat{0} & \hat{0} & \hat{I}_B \end{pmatrix} - (-i\gamma_B) \begin{pmatrix} \hat{0} & \hat{0} & \hat{0} \\ \hat{0} & \hat{0} & \hat{0} \\ \hat{0} & \hat{0} & \hat{I}_B \end{pmatrix}\right] = -2\gamma_B \begin{pmatrix} \hat{0} & \hat{0} & \hat{0} \\ \hat{0} & \hat{0} & \hat{0} \\ \hat{0} & \hat{0} & \hat{I}_B \end{pmatrix}.$$

Hence, the retarded Green's function of the device is given by:

$$\widehat{G}_d^R = \left[E\hat{I} - \hat{h}_d - \hat{\Sigma}_B^R - \hat{\Sigma}_T^R\right]^{-1}$$

$$= \begin{pmatrix} (E - i\gamma_T)\hat{I}_T - \hat{h}_T^d & -\hat{v}_{TC}^d & -\hat{v}_{TB}^d \\ -\hat{v}_{CT}^d & E\hat{I}_C - \hat{h}_C^d & -\hat{v}_{CB}^d \\ -\hat{v}_{BT}^d & -\hat{v}_{BC}^d & (E - i\gamma_B)\hat{I}_B - \hat{h}_B^d \end{pmatrix}^{-1}.$$

And the corresponding advanced Green's function is:

© 2016 Macmillan Publishers Limited. All rights reserved.

$$\hat{G}_d^A = \left(\hat{G}_d^R\right)^\dagger = \left[\left(E\hat{I} - \hat{h}_d - \hat{\Sigma}_B^R - \hat{\Sigma}_T^R\right)^{-1}\right]^\dagger = \left[\left(E\hat{I} - \hat{h}_d - \hat{\Sigma}_B^R - \hat{\Sigma}_T^R\right)^\dagger\right]^{-1}$$

$$= \left[\left(E\hat{I}^\dagger - \hat{h}_d^\dagger - \hat{\Sigma}_B^{R\dagger} - \hat{\Sigma}_T^{R\dagger}\right)\right]^{-1} = \left[\left(E\hat{I} - \hat{h}_d - \hat{\Sigma}_B^{R*} - \hat{\Sigma}_T^{R*}\right)\right]^{-1}$$

$$= \left[\left(E\hat{I} - \hat{h}_d - \hat{\Sigma}_B^R - \hat{\Sigma}_T^R\right)^*\right]^{-1} = \left[\left(E\hat{I} - \hat{h}_d - \hat{\Sigma}_B^R - \hat{\Sigma}_T^R\right)^{-1}\right]^* = \left(\hat{G}_d^R\right)^*.$$

Here, we have used the fact that for an invertible matrix $\hat{A}$ we may write $\hat{A}^{-1}\hat{A} = \hat{I}$ and hence $\hat{A}^\dagger\left(\hat{A}^{-1}\right)^\dagger = \left(\hat{A}^{-1}\hat{A}\right)^\dagger = \hat{I}^\dagger = \hat{I}$, such that $\left(\hat{A}^{-1}\right)^\dagger = \hat{A}^{\dagger-1}$ and a similar relation holds for the complex conjugation of an inverse matrix.

We may now use the cyclic property of the trace formula to transform to the basis that diagonalizes $\hat{G}_d^{R/A}$. To this end, we mark by $\hat{U}$ the transformation matrix that diagonalizes $\hat{H}_d \equiv \hat{h}_d + \hat{\Sigma}_B^R + \hat{\Sigma}_T^R$ such that $\hat{\hat{H}}_d = \hat{U}^{-1}\hat{H}_d\hat{U}$ is a diagonal matrix (assuming diagonalizability). Since $\hat{H}_d$ is a complex symmetric matrix $\hat{U}$ is complex orthogonal such that $\hat{U}^\dagger = \hat{U}^{-1^*}$ or $\hat{U}^T = \hat{U}^{-1}$. With this we define:

$$\hat{\hat{G}}_d^R \equiv \hat{U}^{-1}\hat{G}_d^R\hat{U} = \hat{U}^{-1}\left(E\hat{I} - \hat{h}_d - \hat{\Sigma}_B^R - \hat{\Sigma}_T^R\right)^{-1}\hat{U} = \hat{U}^{-1}\left(E\hat{I} - \hat{H}_d\right)^{-1}\hat{U}$$

$$= \left[\hat{U}^{-1}\left(E\hat{I} - \hat{H}_d\right)\hat{U}\right]^{-1} = \left[E\hat{U}^{-1}\hat{I}\hat{U} - \hat{U}^{-1}\hat{H}_d\hat{U}\right]^{-1} = \left[E\hat{I} - \hat{\hat{H}}_d\right]^{-1}$$

$$= \begin{pmatrix} \frac{1}{E-\varepsilon_d^1} & 0 & 0 \\ 0 & \ddots & 0 \\ 0 & 0 & \frac{1}{E-\varepsilon_d^n} \end{pmatrix},$$

where $\{\varepsilon_d^i\}$ are the eigenvalues of $\hat{\hat{H}}_d$ and we have used the following relation for the inverse of a matrix multiplication $\left(\hat{A}\hat{B}\hat{C}\right)^{-1} = \hat{C}^{-1}\hat{B}^{-1}\hat{A}^{-1}$.

Similarly, we may write:

$$\hat{\hat{G}}_d^A \equiv \hat{U}^{-1^*}\hat{G}_d^A\hat{U}^* = \hat{U}^{-1^*}\left(\hat{G}_d^R\right)^*\hat{U}^* = \left(\hat{U}^{-1}\hat{G}_d^R\hat{U}\right)^* = \hat{\hat{G}}_d^{R^*} = \begin{pmatrix} \frac{1}{E-\varepsilon_d^{1^*}} & 0 & 0 \\ 0 & \ddots & 0 \\ 0 & 0 & \frac{1}{E-\varepsilon_d^{n^*}} \end{pmatrix}.$$

Hence, the trace formula for the transmittance probability can be rewritten as follows:

$$T(E) = Tr\left[\hat{G}_d^R\hat{\Gamma}_B\hat{G}_d^A\hat{\Gamma}_T\right] = Tr\left[\hat{U}\hat{U}^{-1}\hat{G}_d^R\hat{U}\hat{U}^{-1}\hat{\Gamma}_B\left(\hat{U}\hat{U}^{-1}\right)^*\hat{G}_d^A\left(\hat{U}\hat{U}^{-1}\right)^*\hat{\Gamma}_T\right]$$

$$= Tr\left[\hat{U}\hat{U}^{-1}\hat{G}_d^R\hat{U}\hat{U}^{-1}\hat{\Gamma}_B\hat{U}^*\hat{U}^{-1^*}\hat{G}_d^A\hat{U}^*\hat{U}^{-1^*}\hat{\Gamma}_T\right]$$

$$= Tr\left[\left(\hat{U}^{-1}\hat{G}_d^R\hat{U}\right)\left(\hat{U}^{-1}\hat{\Gamma}_B\hat{U}^*\right)\left(\hat{U}^{-1^*}\hat{G}_d^A\hat{U}^*\right)\left(\hat{U}^{-1^*}\hat{\Gamma}_T\hat{U}\right)\right],$$

© 2016 Macmillan Publishers Limited. All rights reserved.

 DOI: 10.1038/NNANO.2016.85

where we have used the cyclic property of the trace. We may now define $\hat{\hat{\Gamma}}_B \equiv \hat{U}^{-1}\hat{\Gamma}_B\hat{U}^* = \hat{U}^T\hat{\Gamma}_B\hat{U}^*$ and $\hat{\hat{\Gamma}}_T \equiv \hat{U}^{-1^*}\hat{\Gamma}_T\hat{U} = \hat{U}^\dagger\hat{\Gamma}_T\hat{U}$. Since $\hat{\Gamma}_B$ and $\hat{\Gamma}_T$ are diagonal matrices the matrix elements of $\hat{\hat{\Gamma}}_B$ and $\hat{\hat{\Gamma}}_T$ can be easily calculated as:

$$\left(\hat{\hat{\Gamma}}_B\right)_{ij} = \sum_k\sum_l \left(\hat{U}^T\right)_{ik}(\hat{\Gamma}_B)_{kl}\left(\hat{U}^*\right)_{lj} = \sum_k\sum_l \left(\hat{U}^T\right)_{ik}(\hat{\Gamma}_B)_{kk}\delta_{kl}\left(\hat{U}^*\right)_{lj}$$
$$= \sum_k \left(\hat{U}^T\right)_{ik}(\hat{\Gamma}_B)_{kk}\left(\hat{U}^*\right)_{kj} = \sum_k (\hat{U})_{ki}(\hat{\Gamma}_B)_{kk}\left(\hat{U}^*\right)_{kj}$$

and

$$\left(\hat{\hat{\Gamma}}_T\right)_{ij} = \sum_k\sum_l \left(\hat{U}^\dagger\right)_{ik}(\hat{\Gamma}_T)_{kl}(\hat{U})_{lj} = \sum_k\sum_l \left(\hat{U}^\dagger\right)_{ik}(\hat{\Gamma}_T)_{kk}\delta_{kl}(\hat{U})_{lj}$$
$$= \sum_k \left(\hat{U}^\dagger\right)_{ik}(\hat{\Gamma}_T)_{kk}(\hat{U})_{kj} = \sum_k \left(\hat{U}^*\right)_{ki}(\hat{\Gamma}_T)_{kk}(\hat{U})_{kj}.$$

Where the sums run only over the non-zero terms in $\hat{\Gamma}_{B/T}$. With this the trace formula can be written as:

$$T(E) = Tr\left[\hat{\hat{G}}_d^R\hat{\hat{\Gamma}}_B\hat{\hat{G}}_d^A\hat{\hat{\Gamma}}_T\right].$$

In terms of the matrix elements this may be written as:

$$T(E) = \sum_i \left[\hat{\hat{G}}_d^R\hat{\hat{\Gamma}}_B\hat{\hat{G}}_d^A\hat{\hat{\Gamma}}_T\right]_{ii} = \sum_i\sum_j\sum_k\sum_l \left[\hat{\hat{G}}_d^R\right]_{ij}\left[\hat{\hat{\Gamma}}_B\right]_{jk}\left[\hat{\hat{G}}_d^A\right]_{kl}\left[\hat{\hat{\Gamma}}_T\right]_{li}$$
$$= \sum_i\sum_j\sum_k\sum_l \left(E-\varepsilon_d^i\right)^{-1}\delta_{ij}\left[\hat{\hat{\Gamma}}_B\right]_{jk}\left(E-\varepsilon_d^{k^*}\right)^{-1}\delta_{kl}\left[\hat{\hat{\Gamma}}_T\right]_{li}$$
$$= \sum_i\sum_k \left(E-\varepsilon_d^i\right)^{-1}\left[\hat{\hat{\Gamma}}_B\right]_{ik}\left(E-\varepsilon_d^{k^*}\right)^{-1}\left[\hat{\hat{\Gamma}}_T\right]_{ki}$$
$$= \sum_i\sum_k \frac{\left[\hat{\hat{\Gamma}}_B\right]_{ik}\left[\hat{\hat{\Gamma}}_T\right]_{ki}}{\left(E-\varepsilon_d^i\right)\left(E-\varepsilon_d^{k^*}\right)}.$$

This final formula was used in the main text to evaluate the interlayer transport properties of graphene bilayers. In the calculations presented therein, we have considered finite graphene bilayers constructed from hexagonally shaped flakes (see right panel of Fig. S10). We adopted the tight-binding Hamiltonian model and parameters from Refs (*4,9*) and assigned a constant broadening factor $(\gamma_T = \gamma_B = \gamma)$ to all atomic sites within each flake to represent the imaginary part of the corresponding lead self-energy.

When starting from the fully eclipsed AA stacking mode and rotating around an axis passing through two vertically aligned atomic centers (Fig. S12A) the calculated profile exhibits a single peak around 21.8° and a double peak around 38.2° in notable

© 2016 Macmillan Publishers Limited. All rights reserved.

agreement (upon vertical shift) with the experimental results (see dashed orange lines in Fig. 2c,d of the main text). While one may argue that the AA stacking mode is energetically unfavorable and hence less likely to serve as a starting rotational configuration, we note that at the twisted configuration, where the system exhibits superlubricity, (*10-12*) small lateral shifts during the rotation process can readily transform between rotational centers.

In Fig. S10 we plot the calculated interlayer conductance (left panels of Fig. S10) of a hexagonal bilayer graphene flake of side length 8.2 nm (right panel of Fig. S10) as function of deviation of the misfit angle from the magic angles of 21.78°, 27.8°, 32.3°, and 38.2°. As can be seen, the conductance peaks around the main magic angles (30°±8.21°) are considerably larger than those appearing at the secondary magic angles which may explain the latter's absence in the experimental results (left panels in Fig. S10.

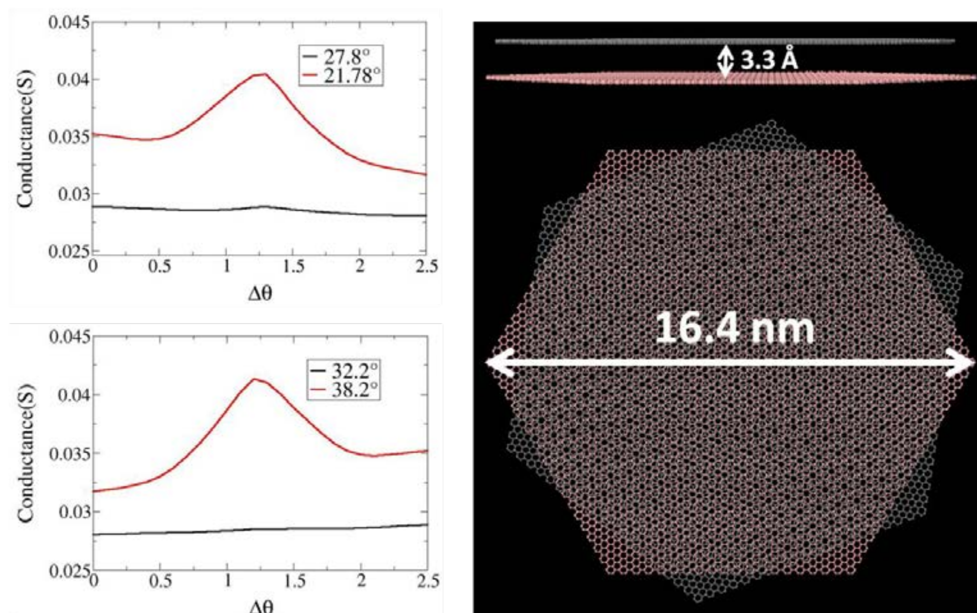

Supplementary Figure 10 | Transverse conductance (left panels) as a function of interlayer misfit angle around several magic angles of increased interlayer commensurability calculated using the descried transport model for a bilayer hexagonal graphene flake of side length 8.2 nm (right panel).

© 2016 Macmillan Publishers Limited. All rights reserved.

DOI: 10.1038/NNANO.2016.85

8. Registry index calculations

Global Registry Index

The registry index (RI) is a concept aimed to quantify the overall inter-layer lattice commensurability in two dimensional (2D) rigid and non-corrugated interfaces with low computational cost. The RI was originally developed to characterize the tribological properties of layered materials where the corrugation of the interlayer sliding energy landscape results mainly from Pauli repulsions between overlapping electron clouds around atoms residing at the two surfaces of the junction. To this end, circles are assigned to each atomic position and the projected overlap between circles of atoms in the two layers serves as a measure for the atomic cloud overlap and hence for the corresponding repulsion (see Fig. S11). Depending on the identity of the material simple expressions that involve sums and differences of the individual overlaps between the various atomic centers are defined. These are then normalized to the range [0:1] such that 0 represents the optimal (in terms of energy) stacking mode and 1 the worst counterpart. The different circle radii can then be tuned to obtain good agreement between the RI and sliding energy landscapes calculated via density functional theory calculations. Specifically, in graphite the circle radii are chosen to be half the bond length and the RI values of 0 and 1 are obtained at the AB and AA stacking modes, respectively (see Fig. S11).

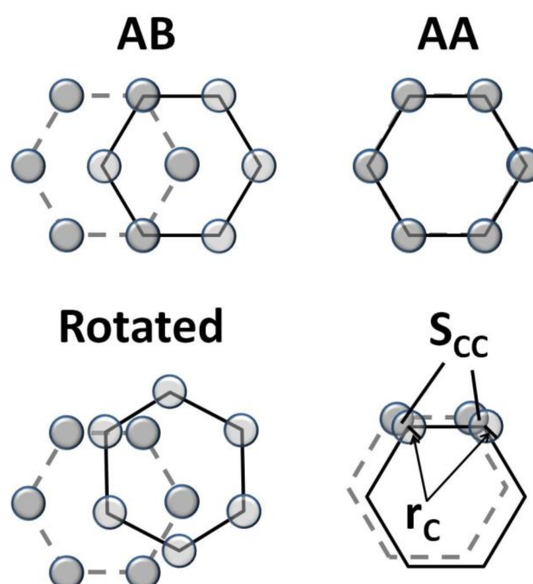

© 2016 Macmillan Publishers Limited. All rights reserved.

Supplementary Figure 11 | Definition of the projected circle overlap (lower right panel) used in the transport adaptation of the registry index of bilayer graphene. Maximal overlap is obtained at the AA (worst in terms of total energy) stacking mode (upper right panel), intermediate overlap is obtained at the AB (optimal) stacking mode (upper left panel), and vanishing overlap is obtained at highly incommensurate shifted and rotated configurations (lower left panel).

Since interlayer electronic transport in multi-layered graphene requires tunneling through a large (~3.33 Å) vacuum barrier one may expect that p_z orbital overlap is a dominant factor here as well. Hence, we can adopt the RI concept to evaluate the dependence of the interlayer transport on the stacking mode of bilayer graphene. At the worst stacking mode, where Pauli repulsions are the highest, maximal orbital overlap is obtained and hence transport is enhanced. However, as one deviates from the AA configuration, by either interlayer sliding or rotation, the interlayer tunneling probability is found to be more sensitive to the orbital overlap (and hence to the lateral position matching of the atoms) than the repulsive interactions dictating the tribological properties. Hence, in order to take this higher sensitivity into account we use a smaller circle radius of $r_C = 0.1 \cdot r_{CC}$ where $r_{CC} = 1.42$ Å is the carbon-carbon bond length in graphene. This allows us to clearly identify interlayer configurations with higher commensurability that present an overall increase of p_z orbital overlap and hence are expected to exhibit enhanced transport.

Similar to the tribological definition of the RI in transport calculations we define the global RI (GRI) to be proportional to the overall projected overlap $RI_{graphite} \sim S_{cc}$, as well. Since the circle radius is chosen to be smaller in this case, the normalized expression differs somewhat and is given by $RI_{graphite} = S_{cc}/S_{cc}^{AA}$, where S_{cc}^{AA} is the overall projected overlap at the AA stacking mode. This term obtains the value of 1 at the AA stacking mode, where the overall projected overlap (and hence interlayer transport) is maximal, and the value of 0 at interlayer configurations were the overlap vanishes. This definition was used to produce Fig. 3b in the main text. A similar concept was developed by Bistritzer and MacDonald to characterize interlayer carrier density overlaps in momentum-space (*13*).

Fig. S12B presents the GRI calculated as a function of misfit angle for two graphene bilayer flake diameters (12 nm – lower panels, 100 nm – upper panels). The flakes that are initially staked at the AB (left panels) or AA (right panels) mode are rotated

© 2016 Macmillan Publishers Limited. All rights reserved.

DOI: 10.1038/NNANO.2016.85

around an axis perpendicular to the basal planes of the layers and passing through two eclipsed atomic sites (full black line) or through an atomic site of one layer residing atop a hexagon center of the other layer (full red line) as shown in Fig. S12A. As can be seen, regardless of the flake dimension, its initial configuration, and the rotational axis sharp conductance peaks appear at the various magic angles discussed in the main text. This signifies the robustness of the enhanced geometric commensuration occurring at these angles for hexagonal lattices and suggests that transport peaks should appear at these angles regardless of the detailed microscopic configuration of the junction. The peaks absolute heights and the ratio between them do vary as a function of the initial stacking mode and the choice of rotational axis with the largest changes being observed for the main peaks at 0° and 60°. When the rotational axis is chosen to be at a hexagon center the RI diagram has mirror symmetry around the misfit angle of 30° whereas for the atom-centered rotational axis this symmetry is lifted. Finally, we note that the width of the RI peaks depends on the flake dimensions becoming narrower with increasing flake diameter (see insets of Fig. S12B).

© 2016 Macmillan Publishers Limited. All rights reserved.

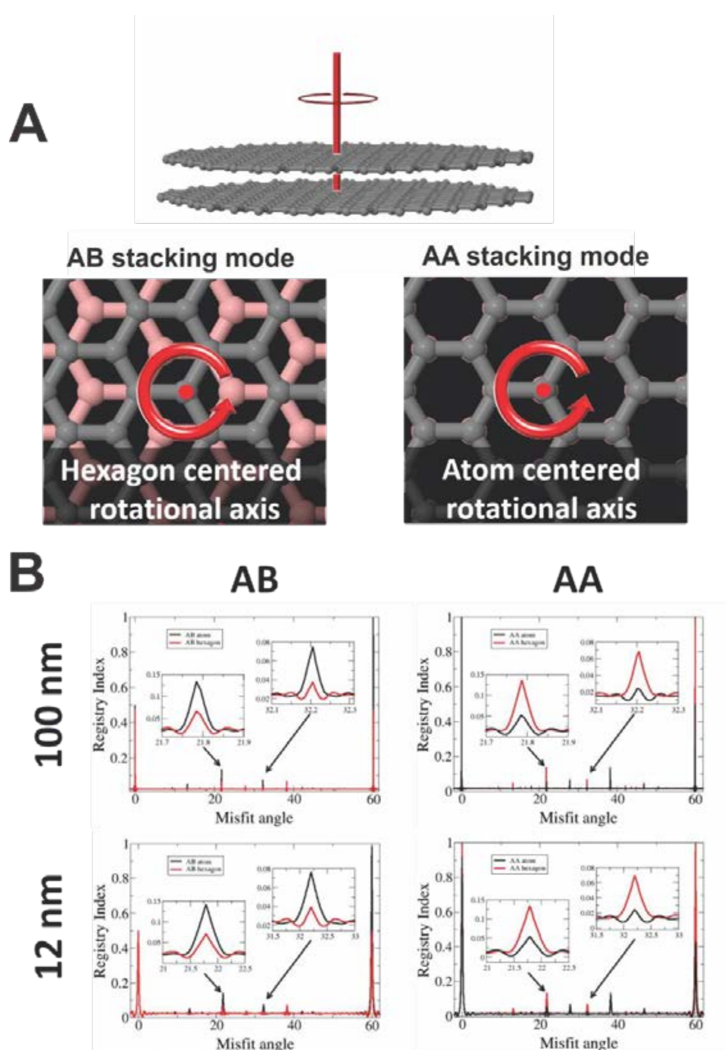

Supplementary Figure 12 | (**A**) Illustration of the two rotational axes considered including a general side view of the bilayer flake, the hexagon centered rotational axis used for the AB stacked bilayer (left), and the atom centered rotational axis used for the AA configuration (right). Lower layer atoms are colored in pink for clarity**.** (**B**) Global registry index as a function of misfit angle for a 12 nm (lower panels) and a 100 nm (upper panels) bilayer graphene flake initially stacked at the AB (left panels) or AA (right panels) mode and rotated around an axis perpendicular to the basal planes of the layers and passing through two eclipsed atomic sites (full black line) or through an atomic site of one layer residing atop a hexagon center of the other layer (full red line). Insets: zoom-in on the peaks located at the magic angles of 21.78° and 32.2°.

Local Registry Index

The local registry index (LRI) is an extension of the global RI designed to characterize the local degree of lattice commensurability in 2D non-corrugated rigid interfaces. Like in the GRI approach the LRI is calculated by evaluating projected

© 2016 Macmillan Publishers Limited. All rights reserved.

 DOI: 10.1038/NNANO.2016.85

circle overlaps. In the present application of the LRI for transport calculations in graphite each atomic center is assigned a value ranging from 0 (designating no overlap with underlying atoms) to 1 (indicating a fully eclipsed atomic center) according to the following normalized expression: $LRI_{graphite} = S_{cc}/S_{cc}^{atom}$. Here, S_{cc} is the overlap between the circle of radius $r_C = 0.1 \cdot r_{CC}$ assigned to a specific atom and all similar circles of the underling layer and $S_{cc}^{atom} = \pi r_C^2$ is the area of this circle. To visualize the LRI for a given interlayer stacking mode we plot one of the two layers and color each atom according to the value of its LRI (see Fig. S13).

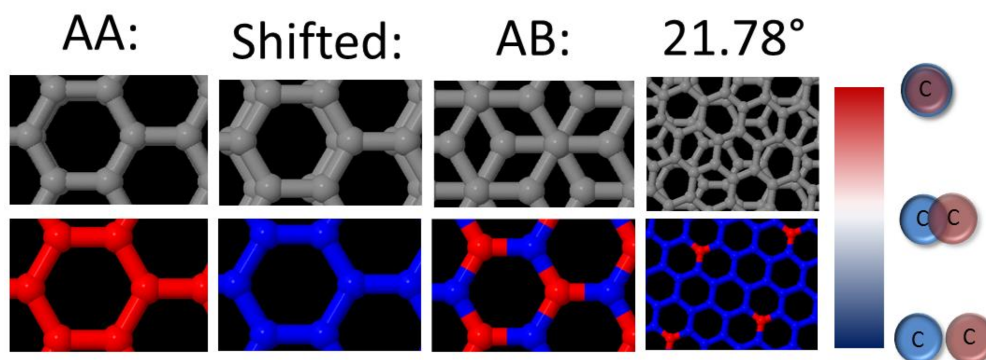

Supplementary Figure 13 | Illustration of the local registry index (LRI) representation for transport calculations in bilayer graphene at the AA (left column), shifted (second column), AB (third column), and rotated (fourth column) interlayer stacking modes. Upper panels show the atomic configurations whereas lower panels present the corresponding LRI map. The color code (right panel) runs from red (representing fully eclipsed interlayer atomic sites) to blue (representing a non-overlapping atomic center).

© 2016 Macmillan Publishers Limited. All rights reserved.

References

1. E. Koren, E. Lörtscher, C. Rawlings, A. W. Knoll, U. Duerig, Adhesion and friction in mesoscopic graphite contacts. *Science*. **348**, 679–683 (2015).

2. E. Koren, A. W. Knoll, E. Lörtscher, U. Duerig, Direct experimental observation of stacking fault scattering in highly oriented pyrolytic graphite meso-structures. *Nat. Commun.* **5**, 5837 (2014).

3. E. Koren, A. W. Knoll, E. Lörtscher, U. Duerig, Meso-scale measurement of the electrical spreading resistance in highly anisotropic media. *Appl. Phys. Lett.* **105**, 123112 (2014).

4. V. Perebeinos, J. Tersoff, P. Avouris, Phonon-Mediated Interlayer Conductance in Twisted Graphene Bilayers. *Phys.Rev.Lett.* **109**, 096602 (2012), doi:10.1103/PhysRevLett.109.236604.

5. J. M. B. Lopes dos Santos, N. M. R. Peres, A. H. Castro Neto, Graphene Bilayer with a Twist: Electronic Structure. *Phys.Rev.Lett.* **99**, 256802 (2007), doi:10.1103/PhysRevLett.99.256802.

6. S. Datta, *Quantum transport: atom to transistor* (Cambridge University Press, 2005).

7. D. Walter, D. Neuhauser, R. Baer, Quantum interference in polycyclic hydrocarbon molecular wires. *Chem. Phys.* **299**, 139–145 (2004).

8. O. Hod, E. Rabani, R. Baer, Magnetoresistance of Nanoscale Molecular Devices. *Acc. Chem. Res.* **39**, 109–117 (2006).

9. K. M. M. Habib, S. S. Sylvia, S. Ge, M. Neupane, R. K. Lake, The coherent interlayer resistance of a single, rotated interface between two stacks of AB graphite. *Appl. Phys. Lett.* **103**, 243114 (2013).

10. M. Dienwiebel *et al.*, Superlubricity of Graphite. *Phys. Rev. Lett.* **92,** 126101 (2004), doi:10.1103/PhysRevLett.92.126101.

11. A. S. de Wijn, A. Fasolino, A. E. Filippov, M. Urbakh, Low friction and rotational dynamics of crystalline flakes in solid lubrication. *EPL Europhys. Lett.* **95**, 66002 (2011).

12. O. Hod, Interlayer commensurability and superlubricity in rigid layered materials. *Phys. Rev. B*. **86,** 075444 (2012), doi:10.1103/PhysRevB.86.075444.

13. R. Bistritzer, A. H. MacDonald, Transport between twisted graphene layers. *Phys. Rev. B*. **81**, 245412 (2010), doi:10.1103/PhysRevB.81.245412.

© 2016 Macmillan Publishers Limited. All rights reserved.